Kriging-Weighted Laplacian Kernels for Grayscale Image Sharpening

TUAN D. PHAM⁰, (Senior Member, IEEE)

Center for Artificial Intelligence, Prince Mohammad Bin Fahd University, Khobar 31952, Saudi Arabia

e-mail: tpham@pmu.edu.sa

ABSTRACT Sharpening filters are used to highlight fine image details, including object edges. However, sharpening filters are very specific to different types of images as they may create undesired edge effects, over-highlight fine details, or emphasize noise. Laplacian, Laplacian of Gaussian, high-boost, unsharp masking filters, and their extended algorithms are among most widely used sharpening spatial filters. This paper introduces a method that integrates anisotropic averaging with the Laplacian kernels for grayscale image sharpening. The proposed methodology is based on the concept of kriging computation in geostatistics for determining optimal interpolation weights in spatial domain. The convolution of kriging and Laplacian kernels is then carried out for image sharpening. Experimental results suggest certain advantages of the proposed linear convolution model for image sharpening over the Laplacian, Laplacian of Gaussian, high-boost, unsharp masking, and anisotropic diffusion methods in terms of the balance of sharpness and natural visualization. Another advantage of the proposed method is that it does not require any input statistical parameters.

INDEX TERMS Image sharpening, convolution, Laplacian operators, geostatistics, ordinary kriging.

I. INTRODUCTION

Sharpened images produced by Laplacian, Laplacian of Gaussian (LoG), unsharp masking, and high-boost filters are based on linear convolution kernels. Image convolution is the process of adding values of a pixel and its neighbors linearly weighted by a filter kernel to every pixel. The purpose of convolution is to modify the spatial characteristics of an image, resulting in, such as smoothing, sharpening, enhancing, or edge highlighting to suit various applications [1]–[4]. In general, the convolution of a kernel k and an image $f(x, y)$ can be expressed as

$$g(x, y) = k \circledast f(x, y) = \sum_{m=-a}^{a} \sum_{n=-b}^{b} k(m, n) f(x - m, y - n),$$

$$(1)$$

where $g(x, y)$ is the output image, and $\circledast$ denotes the convolution operator.

Laplacian filter-based kernels [5], which are edge-sharpening filters, have been utilized in several applications [6]–[15]. The Laplacian operator takes partial derivatives along the two spatial axes of an image $f(x, y)$ and is

defined as [5]

$$\triangledown^2 f(x, y) = \frac{\partial^2 f(x, y)}{\partial x^2} + \frac{\partial^2 f(x, y)}{\partial y^2}$$
$$= f(x + 1, y) + f(x - 1, y) + f(x, y + 1)$$
$$+ f(x, y - 1) - 4f(x, y), \qquad (2)$$

which highlights sharp intensity transitions and reduces the effect of regions having slowly varying gray levels, resulting in the following 3 × 3 Laplacian filters

$$\begin{bmatrix} 0 & 1 & 0 \\ 1 & -4 & 1 \\ 0 & 1 & 0 \end{bmatrix}, \quad \begin{bmatrix} 1 & 1 & 1 \\ 1 & -8 & 1 \\ 1 & 1 & 1 \end{bmatrix},$$

where the left matrix is based on Eq. 2, and the right is an extension of Eq. 2 to include the diagonal elements.

To rectify the effect of featureless image background while sharpness is still reserved can be obtained by subtracting the Laplacian image from the original, giving [5]

$$f^*(x, y) = f(x, y) - \triangledown^2 f(x, y)$$
$$= f(x, y) - [f(x + 1, y) + f(x - 1, y)$$
$$+ f(x, y + 1) + f(x, y - 1) - 4f(x, y)],$$

$$= 5f(x, y) - [f(x + 1, y) + f(x - 1, y)$$
$$+ f(x, y + 1) + f(x, y - 1)], \qquad (3)$$

which results in a 3×3 composite sharpening kernel and its extended version, respectively, as

$$L_1 = \begin{bmatrix} 0 & -1 & 0 \\ -1 & 5 & -1 \\ 0 & -1 & 0 \end{bmatrix}, \quad L_2 = \begin{bmatrix} -1 & -1 & 1 \\ -1 & 9 & -1 \\ -1 & -1 & -1 \end{bmatrix}.$$

Because L_1 and L_2 are derived from the second derivative of an image, which highlights regions of rapid intensity change, both kernels are sensitive to noise. To address this issue, it is suggested to Gaussian-smooth the image before applying the Laplacian. This procedure is known as the LoG, which is defined as [16], [17]

$$\nabla^2 G(x, y) = \frac{1}{\pi \sigma^4} \left(1 - \frac{x^2 + y^2}{2\sigma^2} \right) \exp \left(-\frac{x^2 + y^2}{2\sigma^2} \right), \quad (4)$$

where σ is the standard deviation,

All L_1, L_2, and LoG kernels yield isotropic results. Because an isotropic operator applies the rate of change equally in all directions of an image, it carries no particular sensitivity or bias toward different spatial orientations. An anisotropic topography has directional attributes that may be different at all points or directions of an image. Effort was spent on addressing this issue by minimizing the overall anisotropy produced by Laplacian kernels [18], or using local Laplacian kernels [6], [15].

A high-pass filtered (sharpened) image, denoted as $f_{HP}(x, y)$, can be obtained as

$$f_{HP}(x, y) = f(x, y) - f_{LP}(x, y), \qquad (5)$$

where $f(x, y)$ and $f_{LP}(x, y)$ are original and low-pass filtered (blurred or unsharp) images, respectively. Because of the use of an unsharp image, this process is also known as unsharp masking (UM) [5].

A high-boost filtered image, denoted as $f_{HB}(x, y)$, is defined as

$$f_{HB}(x, y) = \alpha f(x, y) - f_{LP}(x, y), \qquad (6)$$
$$= (\alpha - 1)f(x, y) + f(x, y) - f_{LP}(x, y), \qquad (7)$$
$$= (\alpha - 1)f(x, y) + f_{HP}(x, y), \qquad (8)$$

wkere $\alpha \geq 1$ is a scaling factor.

If the Laplacian image is used as $f_{HP}(x, y)$, then $f_{HB}(x, y)$ is defined as

$$f_{HB}(x, y) = \alpha f(x, y) - \nabla^2 f(x, y), \qquad (9)$$

which gives the following sharpening second-order derivative kernels:

$$H_1 = \begin{bmatrix} 0 & -1 & 0 \\ -1 & \alpha + 4 & -1 \\ 0 & -1 & 0 \end{bmatrix}, \quad H_2 = \begin{bmatrix} -1 & -1 & -1 \\ -1 & \alpha + 8 & -1 \\ -1 & -1 & -1 \end{bmatrix}.$$

If $\alpha = 1$, both high-boost kernels H_1 and H_2 become Laplacian L_1 and L_2, respectively.

Laplacian, LoG, unsharp masking, and high-boost filters, which are benchmark methods for comparing image-sharpening algorithms [19], have been presented herein. Several other methods developed for image sharpening are such as the anisotropic diffusion (AD) filter [20], [21], which iteratively selected the AD coefficient to allow various degrees of smoothing within different image regions and maintain sharpness between region boundaries; the class of iterative morphological operators, which were based on a Laplacian function, was proposed for grayscale image sharpening [22]; fuzzy morphology for enhancing details in historical images [23]. Because wavelet coefficients can reveal high frequency components of an image at multiple resolutions, a wavelet-based algorithm was developed for image sharpening [24]. Histogram equalization [25], which aimed to improve contrast by considering changes in pixel values according to the intensity distribution of the input image, was utilized for sharpening images. The Sobolev isotropic diffusion [26] was developed for image sharpening. This method applied the Sobolev gradients to compute the partial differential equations for image diffusion and sharpening.

Some other methods for image sharpening developed in the past decade include a method using a multi-scale scheme and wavelet discrete transform, where the initial result was processed by unsharp masking filters and the final image produced using a wavelet fusion scheme [27]. Locally adaptive techniques for image sharpening were introduced to achieve "pleasant" visualization when smoothing parameters can be appropriately chosen [28]. An approach for adjusting image sharpness was recently proposed by constructing the binding filter, which is based on the Gaussian distribution, to define the kernel weights for combining with the high-boost filter, and the results achieved having properties of both Gaussian smoothing and high-boost filtering [29]. Another recent work [30] implemented the anisotropic diffusion filter [20] with twenty iterations for image smoothing and then used the unsharp masking for image sharpening.

As an attempt to consider anisotropic properties of an image to be convolved with Laplacian kernels, this paper introduces the use of kriging weights as a secondary kernel whose derivation is based on statistical properties of experimental anisotropic semivariograms. Unlike having fixed values of kernel coefficients, the kriging weights vary according to changes in image semivariograms, giving different convolution results in images of different spatial statistics.

The rest of this paper is organized as follows. Section II presents mathematical derivations of the proposed kriging-weighted Laplacian operators. Section III shows several examples to illustrate, compare, and discuss the results obtained from the kriging-weighted Laplacian method with those produced from other image-sharpening models. Finally, Section IV is the conclusion of findings, including remarks

a_1	a_2	a_3
a_4	a_0	a_5
a_6	a_7	a_8

FIGURE 1. A 3× 3 window and spatial locations of pixels for computing kriging estimate of pixel at center.

on some limitations of the proposed method and suggestions of issues for future research.

II. KRIGING-WEIGHTED LAPLACIAN OPERATORS

Let $z(a)$ be a random function of spatial location a, the ordinary kriging holds the following intrinsic hypothesis [31]:

$$E[z(a)] = \mu. \tag{10a}$$

$$Var[z(a) - z(a + h)] = E\left[\{z(a) - z(a + h)\}^2\right] \tag{10b}$$

$$= 2\gamma(h), \tag{10c}$$

where $E[\cdot]$, μ, and $\gamma(\cdot)$ denote expected value, mean, and semivariogram of the random function, respectively; and a and $a + h$ are any two spatial locations separated by distance h.

Let $z(a_i)$ and $z(a_j)$ be the values of two data points at two spatial locations a_i and a_j, respectively. It was shown that [32]

$$\gamma(a_i - a_j) = \gamma(a_i - a) + \gamma(a_j - a)$$
$$-Cov[z(a_i) - z(a), z(a_j) - z(a)]. \tag{11}$$

To derive kriging weights in the setting of the Laplacian operators, let a_0 be the location of $f(x, y)$, a_1 of $f(x-1, y-1)$, a_2 of $f(x, y-1)$, a_3 of $f(x+1, y-1)$, a_4 of $f(x-1, y)$, a_5 of $f(x + 1, y)$, a_6 of $f(x - 1, y+1)$, a_7 of $f(x, y+1)$, and a_8 of $f(x + 1, y + 1)$, which are shown in Fig. 1.

The value of $f(a_0)$ can be predicted using the best linear unbiased estimator of ordinary kriging as [32]

$$\hat{f}(a_0) = \sum_{i=1}^{8} w_i f(a_i), \tag{12}$$

where w_i, $i = 1, \ldots, 8$ are kriging weights that can be optimally determined by minimizing the estimation variance $\sigma^2(a_0)$:

$$\sigma^2(a_0) = Var[\hat{f}(a_0) - f(a_0)]. \tag{13}$$

Using Eq. 12, the estimate is done via the following constrained optimization

$$\sigma^2(a_0) = Var\left[\sum_{i=1}^{8} w_i(f(a_i) - f(a_0))\right], \tag{14}$$

which is subject to $\sum_{i=1}^{8} w_i = 1$. Based on the following proof [32]

$$Var\left[\sum_i w_i z(a_i)\right] = \sum_i \sum_j w_i w_j Cov[z(a_i), z(a_j)], \tag{15}$$

Eq. 14 can be rewritten as

$$\sigma^2(a_0) = \sum_{i=1}^{8} \sum_{j=1}^{8} w_i w_j Cov[f(a_i) - f(a_0), f(a_j) - f(a_0)]. \tag{16}$$

Using Eq. 11,

$$\sigma^2(a_0) = \sum_{i=1}^{8} \sum_{j=1}^{8} w_i w_j [\gamma(a_i - a_0)$$
$$+ \gamma(a_j - a_0) - \gamma(a_i - a_j)] \tag{17a}$$

$$= \sum_{i=1}^{8} w_i \gamma(a_i - a_0) + \sum_{j=1}^{8} w_j \gamma(a_j - a_0)$$

$$- \sum_{i=1}^{8} \sum_{j=1}^{8} w_i w_j \gamma(a_i - a_j) \tag{17b}$$

$$= 2 \sum_{i=1}^{8} w_i \gamma(a_i - a_0) - \sum_{i=1}^{8} \sum_{j=1}^{8} w_i w_j \gamma(a_i - a_j). \tag{17c}$$

The Lagrangian function for ordinary kriging estimate of $f(a_0)$ can be constructed as

$$L(w_1, \ldots, w_8; \lambda) = \sigma_2(a_0) + 2\lambda \left(\sum_{i=1}^{8} w_i - 1\right), \tag{18}$$

where λ is a Lagrange multiplier.

Let $\gamma(a_i - a_j)$ now be denoted as $\gamma_{i,j}$. To minimize the variance of estimation, all first derivatives of the Lagrangian function with respect to w_i, $i = 1, \ldots, 8$, and λ must be set to zero, which are

$$\frac{\partial L(w_1, \ldots, w_8; \lambda)}{\partial w_i} = 2\gamma_{i,0} - 2\gamma_{i,j} + 2\lambda = 0 \tag{19a}$$

$$\frac{\partial L(w_1, \ldots, w_8; \lambda)}{\partial \lambda} = \sum_{i=1}^{8} w_i - 1 = 0 \tag{19b}$$

The above Lagrangian method results in the determination of unique kriging weights by solving the following set of simultaneous equations:

$$\begin{cases} \sum_{i=1}^{8} w_i \gamma_{1,i} - \lambda = \gamma_{1,0} \\ \sum_{i=1}^{8} w_i \gamma_{2,i} - \lambda = \gamma_{2,0} \\ \ldots \\ \sum_{i=1}^{8} w_i \gamma_{8,i} - \lambda = \gamma_{8,0} \\ \sum_{i=1}^{8} w_i = 1 \end{cases} \tag{20}$$

TABLE 1. Derivation of a 3 × 3 anisotropic kriging-weighted kernel.

$$
\mathbf{A} = \begin{bmatrix}
0 & \gamma_{1,2}(\Delta x) & \gamma_{1,3}(\Delta x) & \gamma_{1,4}(\Delta y) & \gamma_{1,5}(\Delta D^{+}) & \gamma_{1,6}(\Delta y) & \gamma_{1,7}(\Delta D^{+}) & \gamma_{1,8}(\Delta D^{+}) & 1 \\
 & 0 & \gamma_{2,3}(\Delta x) & \gamma_{2,4}(\Delta D^{-}) & \gamma_{2,5}(\Delta D^{+}) & \gamma_{2,6}(\Delta D^{-}) & \gamma_{2,7}(\Delta y) & \gamma_{2,8}(\Delta D^{+}) & 1 \\
 & & 0 & \gamma_{3,4}(\Delta D^{-}) & \gamma_{3,5}(\Delta y) & \gamma_{3,6}(\Delta D^{-}) & \gamma_{3,7}(\Delta D^{-}) & \gamma_{3,8}(\Delta y) & 1 \\
 & & & 0 & \gamma_{4,5}(\Delta x) & \gamma_{4,6}(\Delta y) & \gamma_{4,7}(\Delta D^{+}) & \gamma_{4,8}(\Delta D^{+}) & 1 \\
 & & & & 0 & \gamma_{5,6}(\Delta D^{-}) & \gamma_{5,7}(\Delta D^{-}) & \gamma_{5,8}(\Delta y) & 1 \\
 & & & & & 0 & \gamma_{6,7}(\Delta x) & \gamma_{6,8}(\Delta x) & 1 \\
 & & & & & & 0 & \gamma_{7,8}(\Delta x) & 1 \\
 & & & & & & & 0 & 1 \\
 & & & & & & & & 0
\end{bmatrix}
$$

$$
\mathbf{w} = \begin{bmatrix} w_1 & w_2 & w_3 & w_4 & w_5 & w_6 & w_7 & w_8 & -\lambda \end{bmatrix}^{T}
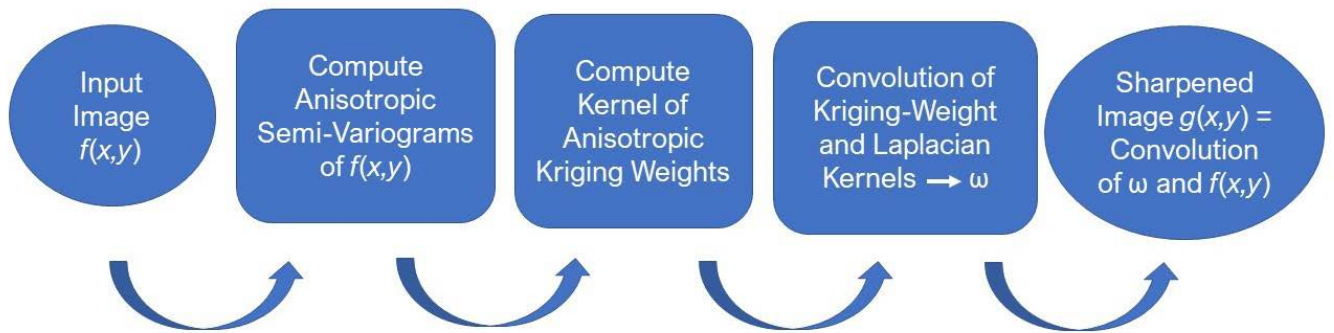$$

$$
\mathbf{b} = \begin{bmatrix} \gamma_{1,0}(\Delta D^{+}) & \gamma_{2,0}(\Delta y) & \gamma_{3,0}(\Delta D^{-}) & \gamma_{4,0}(\Delta x) & \gamma_{5,0}(\Delta x) & \gamma_{6,0}(\Delta D^{-}) & \gamma_{7,0}(\Delta y) & \gamma_{8,0}(\Delta D^{+}) & 1 \end{bmatrix}^{T}
$$

FIGURE 2. Graphical procedure for grayscale image sharpening using kriging-weighted Laplacian method.

To consider anisotropy in the semivariogram model, the experimental semivariogram measured in the horizontal direction of an image can be expressed as

$$
\gamma(\Delta x) = \frac{1}{2N(\Delta x)} \sum_{\Delta x} [f(x, y) - f(x + \Delta x, y)]^2, \quad (21)
$$

where $N(\Delta x)$ is the number of pixel pairs separated by Δx.

Likewise, for the vertical direction, the experimental semivariogram can be defined as

$$
\gamma(\Delta y) = \frac{1}{2N(\Delta y)} \sum_{\Delta y} [f(x, y) - f(x, y + \Delta y)]^2, \quad (22)
$$

where $N(\Delta y)$ is the number of pixel pairs separated by Δy.

For a matrix, the main diagonal is the line of elements running from the top-left to bottom-right corners; whereas the antidiagonal is the line of elements running from the top-right to bottom-left corners. Let ΔD^{+} and ΔD^{-} indicate $(\Delta x, \Delta y)$ measured in the directions of the main diagonal and antidiagonal of an image, respectively. The experimental semivariograms measured in the main diagonal and antidiagonal directions can be obtained, respectively, as

$$
\gamma(\Delta D^{+}) = \frac{1}{2N(\Delta D^{+})} \sum_{\Delta D^{+}} [f(x, y) - f(x + \Delta x, y + \Delta y)]^2, \quad (23)
$$

where $N(\Delta D^{+})$ is the number of pixel pairs separated by $(\Delta x, \Delta y)$ in the main-diagonal direction, and

$$
\gamma(\Delta D^{-}) = \frac{1}{2N(\Delta D^{-})} \sum_{\Delta D^{-}} [f(x, y) - f(x - \Delta x, y + \Delta y)]^2, \quad (24)
$$

where $N(\Delta D^{-})$ is the number of pixel pairs separated by $(\Delta x, \Delta y)$ in the antidiagonal direction.

Using the form of Eq. 20, the kriging weights can be determined by solving for $\mathbf{w}$ in the following ordinary kriging system represented in matrix form as

$$
\mathbf{Aw} = \mathbf{b}, \quad (25)
$$

where $\mathbf{A}$, $\mathbf{w}$, and $\mathbf{b}$ are given in Table 1. It can be seen that $\mathbf{A}$ and $\mathbf{b}$ consist of statistical distances that incorporate anisotropy, spatial correlation, and clustering information; and therefore provide the set of weights in terms of spatial continuity [33].

As a result, the 3 × 3 kriging-weighted kernel for Laplacian filter L_2 is of variable coefficients, depending on the anisotropic semivariogram of an image, where, being similar to the Laplacian kernel, the weight at the kernel center is set to -1 to impose that the sum of all elements of the kernel is zero so that the convolution of a homogeneous region is zero. Likewise, the kriging-weighted kernel for Laplacian filter L_1 can

TABLE 2. Measures of image sharpness and visual quality of "Moon", "Lena", "Bridge", and "Nature" images.

Attributes	Original	L_1	H_1	ω_1	L_2	H_2	ω_2	LoG	UM1	UM2	AD1	AD2
					"Moon" image							
Sharpness	3.56	7.50	8.82	5.06	3.68	14.30	5.74	4.51	4.45	4.14	5.36	3.94
$\lvert\Delta_r\rvert$	0	1.11	1.48	0.42	0.04	3.02	0.61	0.27	0.25	0.16	0.51	0.11
No-Reference Quality Metrics												
PIQE	23.14	19.90	57.01	37.95	54.28	57.01	35.06	27.47	28.92	26.93	58.40	63.67
Full-Reference Quality Metrics												
MSE	N/A	52.24	1.16e3	9.96	325.96	1.16e3	25.24	138.57	6.38	29.68	4.47	36.23
PSNR	N/A	30.95	17.50	38.15	23.00	0.02	34.11	26.71	40.08	33.41	41.63	32.54
SSIM	N/A	0.80	0.67	0.91	0.53	0.00	0.84	0.71	0.98	0.95	0.96	0.81
					"Lena" image							
Sharpness	15.80	15.96	31.66	20.45	22.49	43.81	20.11	17.10	15.90	15.81	16.53	16.89
$\lvert\Delta_r\rvert$	0	0.01	1.00	0.29	0.42	1.77	0.27	0.08	0.01	0.00	0.05	0.07
No-Reference Quality Metrics												
PIQE	50.87	46.57	59.30	53.86	59.50	59.30	53.01	53.04	51.19	50.92	46.45	46.33
Full-Reference Quality Metrics												
MSE	N/A	790.38	3.74e3	168.68	3.10e3	3.74e3	253.98	1.68e3	64.75	223.51	39.32	315.86
PSNR	N/A	19.15	0.01	25.86	0.01	0.01	24.08	0.02	30.02	24.64	32.19	23.24
SSIM	N/A	0.67	0.00	0.96	0.00	0.00	0.93	0.00	0.96	0.91	0.95	0.77
					"Bridge" image							
Sharpness	7.54	7.63	20.42	8.65	13.72	31.03	9.77	9.19	7.81	7.87	7.56	8.13
$\lvert\Delta_r\rvert$	0	0.01	1.71	0.15	0.82	3.12	0.30	0.22	0.04	0.04	0.00	0.08
No-Reference Quality Metrics												
PIQE	54.17	43.52	64.19	56.67	72.00	64.19	53.65	61.62	56.11	56.54	55.74	57.81
Full-Reference Quality Metrics												
MSE	N/A	541.64	3.28e3	60	1.74e3	3.28e3	170.65	987.49	52.81	146.23	51.86	432.80
PSNR	N/A	20.79	0.01	30.33	0.02	0.01	25.81	18.19	30.90	26.48	30.98	21.77
SSIM	N/A	0.69	0.00	0.98	0.00	0.00	0.96	0.63	0.96	0.92	0.93	0.74
					"Nature" image							
Sharpness	10.87	12.42	33.92	15.60	25.64	50.44	11.12	15.58	11.82	11.54	11.33	12.53
$\lvert\Delta_r\rvert$	0	0.14	2.12	0.44	1.36	3.64	0.02	0.43	0.09	0.06	0.04	0.15
No-Reference Quality Metrics												
PIQE	44.16	41.10	67.10	44.29	64.72	67.10	44.53	52.12	48.01	46.86	55.81	61.25
Full-Reference Quality Metrics												
MSE	N/A	752.30	3.53e3	273.44	2.91e3	3.53e3	25.94	1.32e3	53.68	139.48	48.43	381.94
PSNR	N/A	19.37	0.01	23.76	0.01	0.01	34.00	0.02	30.83	26.69	31.28	22.31
SSIM	N/A	0.50	0.00	0.86	0.00	0.00	0.98	0.00	0.94	0.89	0.92	0.69

be constructed by considering only $f(a_2)$, $f(a_4)$, $f(a_5)$, and $f(a_7)$ for the estimate of $f(a_0)$ to compute corresponding w_1^*, w_2^*, w_3^*, and w_4^*, respectively, $\sum_{i=1}^{4} w_i^* = 1$; whereas weights for the diagonal elements are set to zero. The corresponding kriging system yields $\mathbf{A}^*$, $\mathbf{w}^*$, and $\mathbf{b}^*$ of size 5×5, 5×1, and 5×1, respectively. Thus, kriging-weighted kernels for L_1 and L_2 are defined, respectively, as

$$K_1 = \begin{bmatrix} 0 & w_1^* & 0 \\ w_2^* & -1 & w_3^* \\ 0 & w_4^* & 0 \end{bmatrix}, \quad K_2 = \begin{bmatrix} w_1 & w_2 & w_3 \\ w_4 & -1 & w_5 \\ w_6 & w_7 & w_8 \end{bmatrix}.$$

Because convolution is commutative: $\alpha \circledast \beta = \beta \circledast \alpha$, and associative: $\alpha \circledast (\beta \circledast \kappa) = (\alpha \circledast \beta) \circledast \kappa$, where α, β, and κ are kernels, multistage filtering therefore can be performed in a single operation. Instead of having an image convolved with a Laplacian kernel first, then the result convolved with the kriging-weighted kernel, the convolution of an image with the kriging-weighted Laplacian kernel can be carried out as

$$g(x, y) = \omega_i \circledast f(x, y), \tag{26}$$

where ω_i is a hybrid filter or kriging-weighted Laplacian kernel that is defined as

$$\omega_i = K_i \circledast L_i, \ i = 1, 2. \tag{27}$$

Fig. 2 graphically shows the procedure for sharpening a grayscale image using the proposed kriging-weighted Laplacian method.

TABLE 3. Measures of image sharpness and visual quality of "Albert Einstein" and "Bow" images.

Attributes	Original	L_1	L_2	LoG	H_1	H_2	UM1	UM2	AD1	AD2	ω_1-UM1	ω_1-UM2
					"Albert Einstein" image							
Sharpness	5.17	9.10	24.59	13.82	16.79	16.79	6.57	8.08	7.67	12.82	20.63	22.71
$\|\Delta_r\|$	0	0.76	3.76	1.68	2.25	2.25	0.27	0.56	0.49	1.48	2.99	3.40
No-Reference Quality Metrics												
PIQE	46.72	35.49	52.17	46.32	54.01	54.01	36.47	43.33	44.23	40.02	41.93	47.88
Full-Reference Quality Metrics												
MSE	N/A	78.17	432.66	201.59	2.99e3	2.99e3	8.73	50.69	23.95	205.26	13.56	56.30
PSNR	N/A	29.20	21.77	25.09	0.01	0.01	38.72	31.08	34.34	25.01	36.81	30.63
SSIM	N/A	0.86	0.65	0.76	0.00	0.00	0.98	0.95	0.95	0.78	0.98	0.95
					"Bow" image							
Sharpness	7.46	9.84	29.50	16.51	23.46	23.46	10.15	12.63	11.23	19.00	28.04	30.41
$\|\Delta_r\|$	0	0.32	2.95	1.21	2.15	2.15	0.36	0.69	0.51	1.55	2.76	3.08
No-Reference Quality Metrics												
PIQE	18.47	10.48	43.93	25.29	34.78	34.78	16.34	17.52	26.35	33.40	16.31	17.38
Full-Reference Quality Metrics												
MSE	N/A	169.50	983.27	433.38	2.49e3	2.49e3	20.48	94.56	32.78	288.97	31.38	106.91
PSNR	N/A	25.84	18.20	21.76	0.01	0.01	35.02	28.37	32.97	23.52	33.16	27.84
SSIM	N/A	0.75	0.49	0.60	0.00	0.00	0.97	0.92	0.93	0.72	0.97	0.92

III. RESULTS

Fig. 3 shows the "Moon" image of size 537×358, and its sharpened versions obtained from the Laplacian (L_1 and L_2), LoG, high-boost (H_1 and H_2), kriging-weighted Laplacian (ω_1 and ω_2), unsharp marking (UM1 and UM2), and anisotropic diffusion-based unsharp masking or, for short notation, anisotropic diffusion (AD1 and AD2) filters. For the LoG, $\sigma = 0.5$ and the filter size is 5×5. For the high-boost filtering, $\alpha = 1.5$ was selected. For the unsharp marking, the standard deviation of the Gaussian low-pass filter was chosen as 1 (UM1) and 3 (UM2). For the anisotropic diffusion, AD1 and AD2 indicate the implementation of the unsharp masking with the standard deviation of the Gaussian low-pass filter = 1 and 3, respectively. The Laplacian, LoG, high-boost, and unsharp masking filters were computed using the R2022a Matlab Image Processing Toolbox. The anisotropic diffusion filter was computed using public Matlab codes [34] provided by authors of the work [30].

Here, a measure of sharpness in grayscale images using gradients [35] was adopted to evaluate the performance of different methods for image sharpening. The absolute relative difference in sharpness between the original and a filtered image is defined as $|\Delta_r| = |f - f^*|/f$, where f and f^* are original and filtered images, respectively. While the sharpened images given by the Laplacian, LoG, kriging-weighted Laplacian, unsharp masking, and anisotropic diffusion filters have similar visualizations (measures of sharpness were between 3.68 (L_1) and 7.50 (L_2)); the high-boost operators amplified the average gray levels of the original image, resulting in significantly brightened images (measures of sharpness obtained by $H_1 = 8.82$ and $H_2 = 14.30$).

To observe more distinct differences in image sharpening using the six filters, Figs. 4, 5, and 6 show the 225×225 "Lena", 195×259 "Bridge", and 182×278 "Nature"

images, respectively. Figs. 4, 5, and 6 also show images filtered by the Laplacian, LoG, high-boost, unsharp masking, anisotropic diffusion, and kriging-weighted Laplacian models, where the same filter parameters described earlier were used for the four applicable models.

For the "Lena" image, it can be seen that while L_1, L_2, LoG, H_1 and H_2 sharpened the image (measures of sharpness were between 15.96 given by L_1 and 43.81 given by H_2) but also highlighted pixels of high changes in intensity, yielding undesirable visual effects such as pixels of the eyes and hair; on the other hand, both unsharp masking (sharpness measures of UM1 and UM2 = 15.90 and 15.81, respectively) and anisotropic diffusion (sharpness measures of AD1 and AD2 = 16.53 and 16.89, respectively) filters tended to suppress some highlights of the outer region of the hair; however, ω_1 (sharpness = 20.45) and ω_2 (sharpness = 20.11) kernels provided a sharpened image with a much better visual appearance.

For the "Bridge" image, the high-boost filters amplified the image contrast, yielding almost a white background for the sky and brightened water; L_1, L_2 and LoG produced the least sharpened versions, in which the suspension cable was invisible; UM1, UM2, AD1, AD2, ω_1, and ω_2 provided similar sharpened versions of the original image (measures of sharpness were between 7.56 (AD1) and 9.77 (ω_2)). AD2 can be noticed to yield some highlighted distortion of the vertical cables. The sharpened outputs of ω_1 and ω_2 were balanced between those of the other 5 methods.

For the "Nature" image, L_2 (measure of sharpness = 13.72), and H_2 (measure of sharpness = 50.44) kernels yielded most dominantly noise-sensitive results; LoG (measure of sharpness = 15.58) and ω_1 (measure of sharpness = 15.60) provided similar visualizations. UM1, UM2, AD1, AD2, ω_1, and ω_2 provided similar sharpened images

FIGURE 3. "Moon" image and its sharpened versions provided by Laplacian (L_1 and L_2), LoG, high-boost (H_1 and H_2), unsharp marking (UM1 and UM2), anisotropic diffusion (AD1 and AD2), and kriging-weighted Laplacian kernels (ω_1 and ω_2).

(measures of sharpness were between 11.12 and 15.60). While some noise effect was emphasized by AD2, it can be observed that the ω_2 kernel could balance both sharpness and noise suppression. Similar to the visual effect

of the "Moon" image sharpened by H_1 and H_2, two high-boost filtered "Nature" images show much higher contrasts, where dark pixels of low frequencies were significantly lightened.

FIGURE 4. Original and sharpened images of "Lena", using Laplacian (L_1 and L_2), LoG, high-boost (H_1 and H_2), unsharp marking (UM1 and UM2), anisotropic diffusion (AD1 and AD2), and kriging-weighted Laplacian kernels (ω_1 and ω_2).

Table 2 shows the measures of sharpness and relative sharpness of the "Moon", "Lena", "Bridge", and "Nature" images obtained from the Laplacian, LoG, high boost, unsharp masking, anisotropic diffusion, and kriging-weighted Laplacian methods. It was apparent that the high-boost filters provided the sharpest visualization by highlighting the bright pixels of the images, whereas the kriging-weighted Laplacian filters gave results balanced between the Laplacian and LoG filters. All filtered images increased the sharpness of the original images. While being able to increase sharpness in images, both ω_1 and ω_2 provided results that have the most similar naturally visual appearance to the original images by avoiding over-highlighting fine details with a sharp discontinuity. H_2 yielded highest measures of image sharpness but resulted in the most unnatural visual expression. The LoG filter highlighted the fine details with a lesser degree than the Laplacian filters.
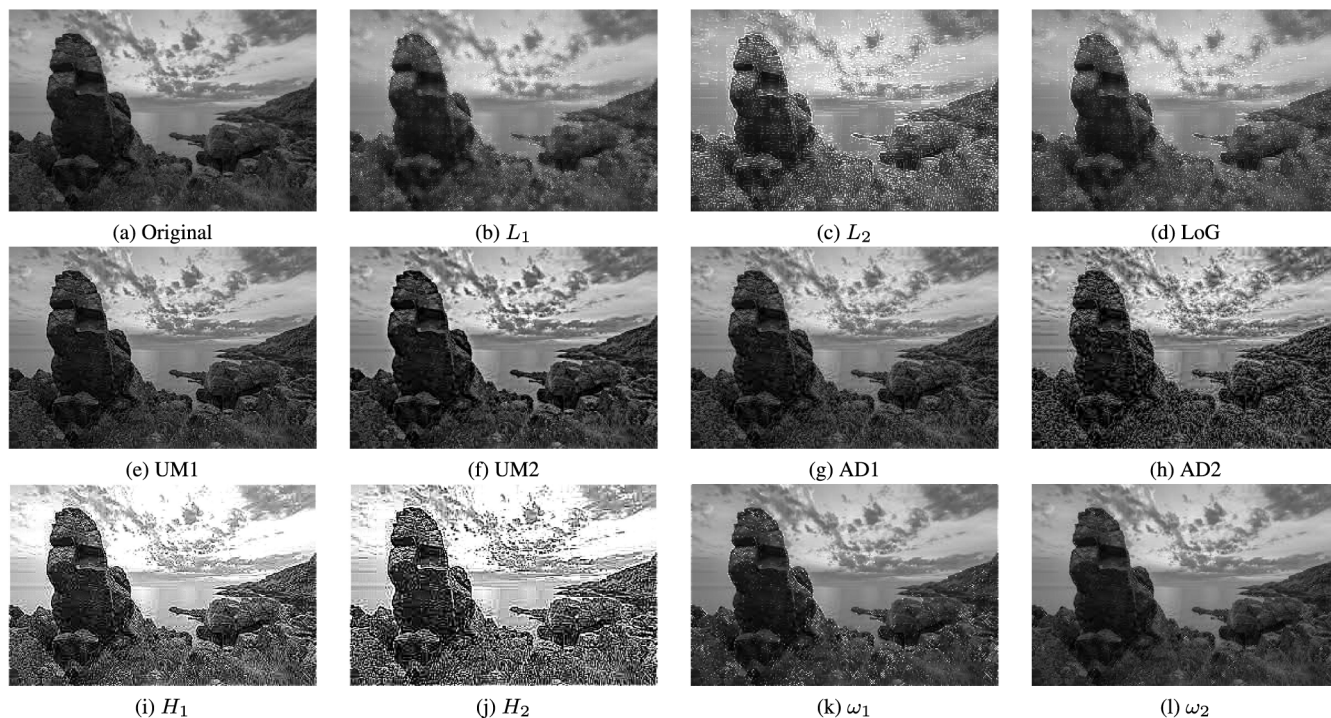
Figs. 7 and 8 show the 182×276 image of "Albert Einstein" and 800×1200 image of a bow (with surrounding landscape) and their sharpened images filtered by different techniques for image sharpening. Because the final result of the anisotropic diffusion (AD1 and AD2) is based on the use of the unsharp masking, the kriging-weighted Laplacian kernel ω_1 was also applied to be further filtered by unsharp masking operators UM1 and UM2, denoted as ω_1-UM1 and ω_1-UM2, for the purpose of comparison of the performance between the two anisotropic methods. Filters L_1, L_2, LoG, H_1, and H_2 produced similar sharpened "Albert Einstein" and "Bow" results as previously discussed for the other four images. In particular, amplification of the image contrast yielded by H_1 and H_2, and unnatural hair as well as facial effects of the "Albert Einstein" output from AD2 can be clearly observed. Combined filters ω_1-UM1 and ω_1-UM2 resulted in the highest measures of sharpness (20.63 and 22.71 respectively for the "Albert Einstein" image, and 28.04 and 30.41 respectively for the "Bow" image) among other filters UM1, UM2, AD1, and AD2. Table 3 shows the measures of sharpness and relative
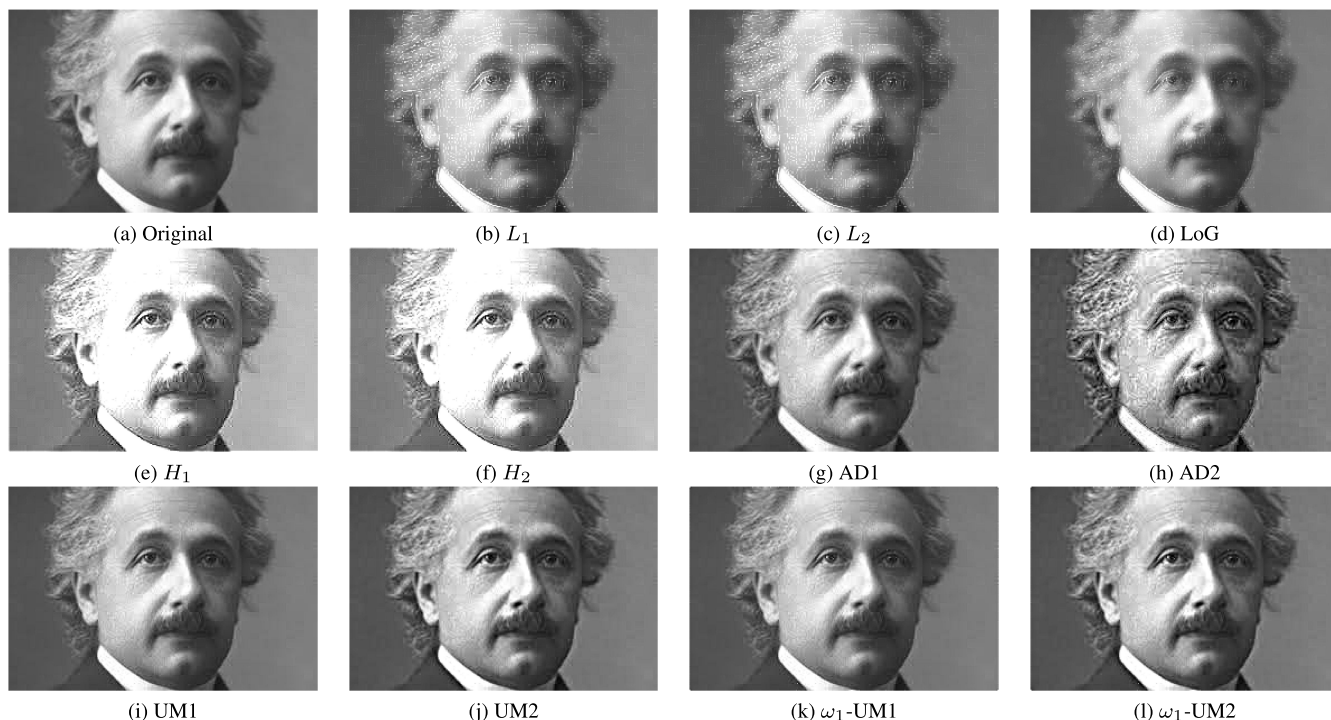
FIGURE 5. Original and sharpened images of "Bridge", using Laplacian (L_1 and L_2), LoG, high-boost (H_1 and H_2), unsharp marking (UM1 and UM2), anisotropic diffusion (AD1 and AD2), and kriging-weighted Laplacian kernels (ω_1 and ω_2).
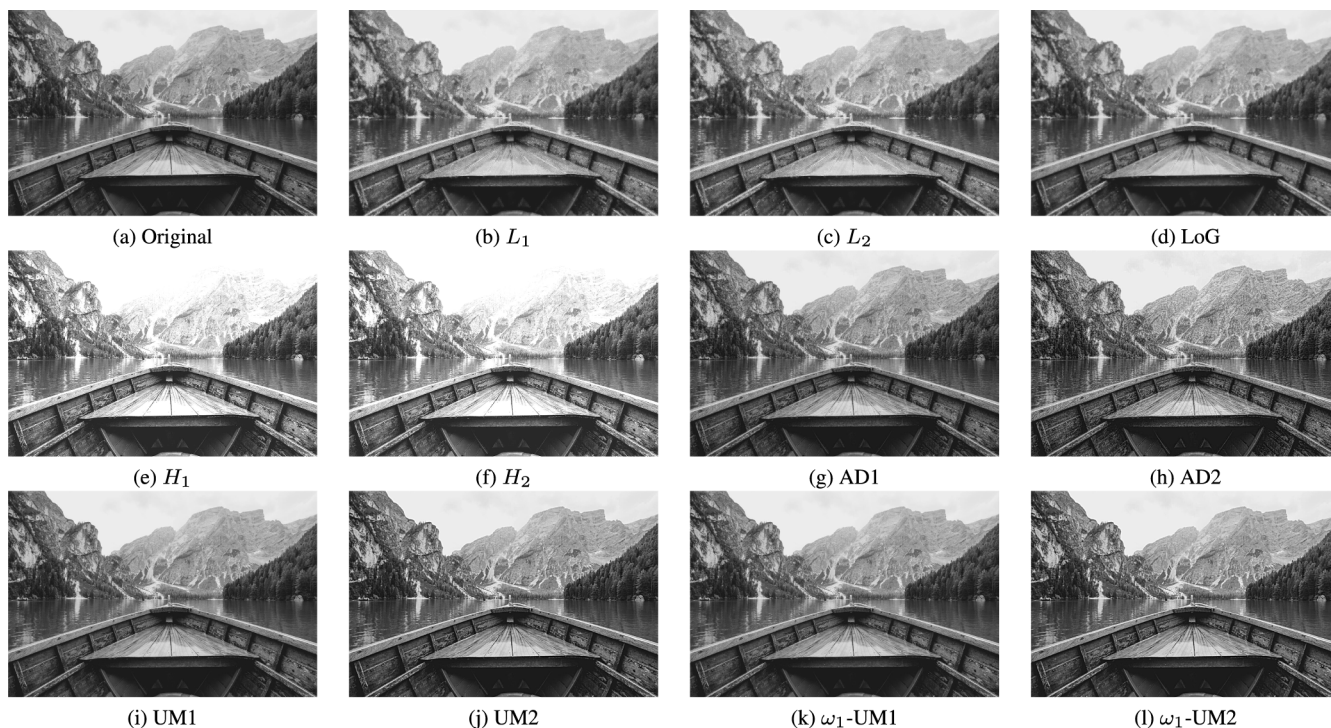

FIGURE 6. Original and sharpened images of "Nature", using Laplacian (L_1 and L_2), LoG, high-boost (H_1 and H_2), unsharp marking (UM1 and UM2), anisotropic diffusion (AD1 and AD2), and kriging-weighted Laplacian kernels (ω_1 and ω_2).

sharpness of these two images obtained from the Laplacian, LoG, high boost, unsharp masking, anisotropic diffusion, and kriging-weighted Laplacian methods.

There are two types of approaches to measure the quality of an image: no-reference quality metrics and full-reference quality metrics. No-reference quality methods compute
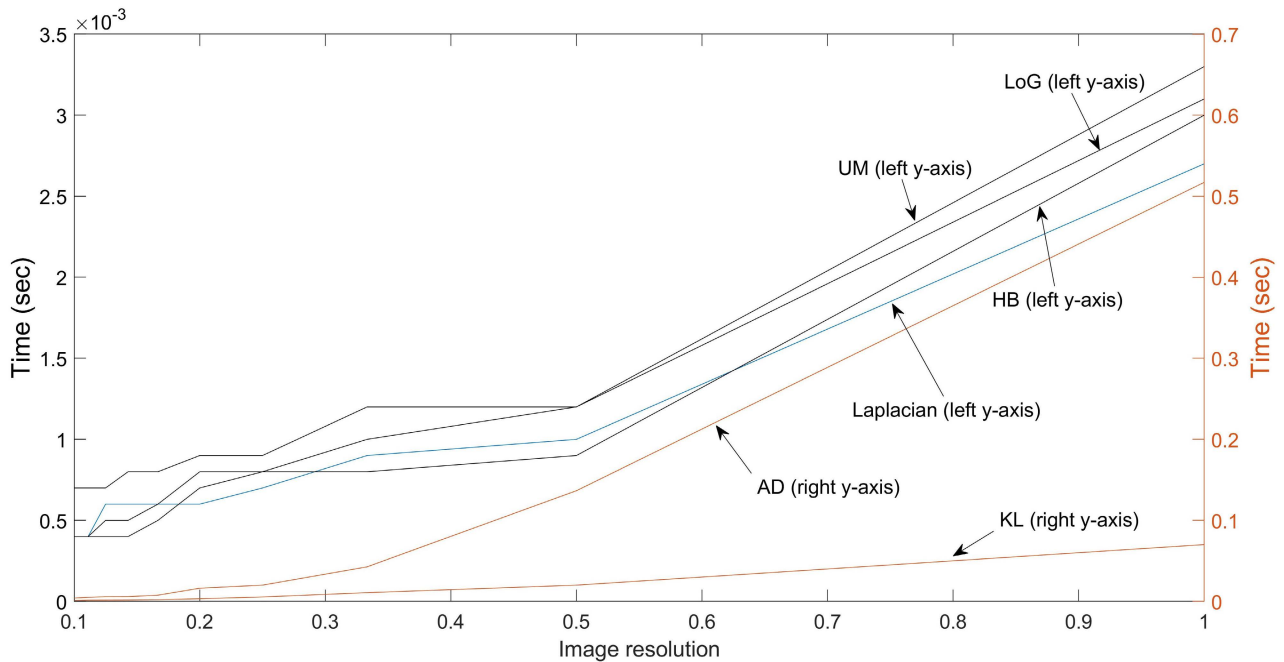
FIGURE 7. "Albert Einstein" image and its sharpened versions provided by Laplacian (L_1 and L_2), LoG, high-boost (H_1 and H_2), anisotropic diffusion (AD1 and AD2), unsharp marking (UM1 and UM2), and combined kriging-weighted Laplacian kernel and unsharp masking (ω_1-UM1 and ω_1-UM2).

FIGURE 8. "Bow" image and its sharpened versions provided by Laplacian (L_1 and L_2), LoG, high-boost (H_1 and H_2), anisotropic diffusion (AD1 and AD2), unsharp marking (UM1 and UM2), and combined kriging-weighted Laplacian kernel and unsharp masking (ω_1-UM1 and ω_1-UM2).

statistical features of an input (either original or filtered) image to assess the image quality. Full-reference algorithms compare the quality between the original and a filtered image. The perception-based image quality evaluator (PIQE) [36], which is a no-reference image-quality metric, were used to

evaluate quality of the images filtered by the Laplacian, LoG, high-boost, and kriging-weighted Laplacian filters. The PIQE score is inversely correlated to the perceptual quality of an image in the range [0, 100]. A lower score indicates higher perceptual image quality.

FIGURE 9. Computational speeds for sharpening the "Bow" image vs. different resolutions required by various operators: Laplacian, Laplacian of Gaussian (LoG), high boost (HB), unsharp masking (UM), anisotropic diffusion (AD), and kriging-weighted Laplacian (KL) filters.

The mean-squared error (MSE), peak signal-to-noise ratio (PSNR), and structural similarity (SSIM) were used as full-reference quality metrics to evaluate the sharpened images. Because the MSE computes the average squared difference between original and filtered pixel values and the PSNR is derived from the MSE, these two measures may not agree well with the human perception of quality. Because the SSIM metric [37] considers local pixel intensities, luminance, and contrast to compute a single local quality score, the SSIM measure is more in alignment with human-based quality scoring. For the SSIM measure, a value closer to 1 indicates better image quality.

Table 2 shows the no-reference and full-reference quality metrics for the "Moon", "Lena", "Bridge", and "Nature" images, and Table 3 shows the no-reference and full-reference quality metrics for the "Albert Einstein" and "Bow" images.

For the "Moon" image, AD2 has the highest (63.67) and L_1 has the lowest (19.90) PIQE scores. The PIQE scores of both ω_1 and ω_2 are between the highest and lowest values, suggesting the balance of visual effect in image sharpness provided by the kriging-weighted Laplacian kernels. For the "Lena", L_2 and AD2 obtained the highest (59.50) and lowest (46.33) PIQE scores, respectively. For the "Bridge", L_2 and L_1 have the highest (72.00) and lowest (43.52) PIQE scores, respectively. For the "Nature", both H_1 and H_2 have the highest PIQE score (67.10), and L_1 has the lowest PIQE score (41.10). Similarly, for the "Albert Einstein" and "Bow" images, both H_1 and H_2 have the highest PIQE score and L_1 has the lowest. Similar observations about the two kriging-weighted Laplacian kernels apply to the other 5 images ("Lena", "Bridge", "Nature", "Albert Einstein" and "Bow" images).

Regarding the MSE and PSNR, both H_1 and H_2 have the highest values, whereas ω_1, ω_2, UM1, UM2, AD1, and AD2 likely have the lowest values for all six images as shown in Figs. 3 – 8.

By means of the SSIM, UM1 has the highest score (0.98) for the "Moon", whereas the score for ω_1 (0.91) is also close to 1; both UM1 and ω_1 have the highest score (0.96) for the "Lena"; ω_1 have the highest score (0.98) for the "Bridge", whereas ω_2 and UM1 have the second highest value (0.96); for the "Nature", ω_2 has the highest score (0.98); UM1 and ω_1-UM1 have the highest scores for both "Albert Einstein" (0.98) and "Bow" (0.97) images. Both H_1 and H_2 have the lowest SSIM scores (0.00), except for the "Moon" image, H_1 scores 0.67. Such results suggest the combination of the kriging-weighted Laplacian and unsharp marking is more favorable than the anisotropic diffusion-based unsharp masking.

The main computational cost for the proposed method is the solving of a system of simultaneous linear equations with either 5 or 9 variables and their associated semivariogram values using either L_1 or L_2, respectively. Such a cost is not high because the computation is done only once, and the times taken for the kriging-weighted Laplacian filter were about 0.03 sec, 0.02 sec, and 0.01 sec longer than the conventional Laplacian, HBF, and LoG filters, respectively, for the images shown in Figs. 4–6, obtained from the central processing unit (CPU) of Intel(R) Core(TM) i7-6500U CPU@2.50GHz. Fig. 9 displays the plot of computational times required by the Laplacian (L_1), HBF (H_1), LoG, unsharp masking (UM1), anisotropic diffusion (AD1), and kriging-weighted Laplacian (ω_1) methods against different resolutions of the "Bow" image performed on the same mentioned computer

hardware, showing the anisotropic diffusion required longest computational time, and the speed for the kriging-weighted Laplacian slowly increased with higher image resolutions.

Edge-sharpening kernels aim to increase the contrast on image edges, that is the darker side of the edge becomes darker and the brighter side brighter; therefore, contrast of the whole image is not affected. As a result, the filtering may lead to edge degradation and other traces such as halos or white artifacts [38] because of sharp transitions in signals. The high-boost filtering raises the high-frequency components of an image by adding more weight to the masked pixels, and therefore can effectively enhance image-shading effects; however, in many cases, it can be very sensitive to noise and magnify unwanted image details. While the Laplacian filtering can restore fine image details, its second-order derivative tend to amplify noise. The LoG is a combination of Laplacian and Gaussian filters, which tries to smooth the original image before applying the Laplacian filter for image sharpening; thus, in some cases, it fails to pick up fine characteristics of an image to a satisfactory level. Results obtained from the unsharp masking and anisotropic diffusion-based unsharp masking can preserve the sharpness of edges better than the Laplacian and LoG methods, but largely depend on the selection of the standard deviation of the Gaussian low-pass filter that may adversely affect the image sharpening if not appropriately selected.

Based on the spatial-statistics properties of an image on its vertical, horizontal, and diagonal directions, the kriging-weighted Laplacian filter derives and convolves the kriging weights with a kernel of second-order derivative for image sharpening. For an isotropic and homogeneous image, it may provide an output similar to the LoG (as in the case of the "Moon" image). For an image of anisotropic content, the kriging-weighted Laplacian filter is able to suppress unwanted details (Lena's hair streaks and "Nature" image), or provide a balanced result between Laplacian, LoG, and high-boost filtering methods ("Bridge" image). For sharpening images of textural content such as the "Lena" and "Albert Einstein" images, the kriging-weighted Laplacian method can provide sharper and more natural visualization than the unsharp masking and anisotropic diffusion-based unsharp masking. Another advantage of the kriging-weighted Laplacian method over the LoG, high-boost, unsharp masking, and anisotropic diffusion filters is that the proposed method is free from statistical parameter specification, which plays a sensitive role to the other models.

IV. CONCLUDING REMARKS

Kriging, which is a geostatistical approach, has been applied to image and signal processing [39]–[44]. An image sharpening filter that incorporates anisotropic information captured by ordinary kriging into the Laplacian filters has been presented. Values of the kriging-weighted kernels are estimated from a spatial variance of an image under study, whose directions of intensity distribution can be of either isotropy or anisotropy.

Results obtained from the foregoing examples have illustrated certain advantages of the kriging-weighted Laplacian method: It is capable of producing filtered images that have sharper visualization than the Laplacian, LoG, unsharp masking, and anisotropic diffusion filters, and less effect of unwanted-detail highlights than the Laplacian, LoG, and high-boost filters. The proposed method can provide results that are of better balance between image sharpness and subjective image quality than the Laplacian, LoG, high-boost, unsharp masking, and anisotropic diffusion filters. In addition, kriging-based kernels of difference sizes can be derived for convolving with other types of filters to suit various applications in image processing. Kriging-based filtering can also be used as adaptive kernels that consider local semivariograms of an image to result in different levels of filtering for modeling structural variability of the image continuity.

Some current limitations of the kriging-weighted Laplacian method are that the computation of the kriging system to determine the optimal kriging weights is based on the experimental anisotropic semi-variograms and applies to only grayscale images. A feasible future work for improving the proposed method would be the consideration of minimization of errors between the experimental anisotropic semivariogram and several theoretical anisotropic semivariogram models for kriging interpolation developed in geostatistics [45] to construct better spatial correlations among intensities and spatial patterns of pixels. Another future work is the extension of the kriging-weighted Laplacian kernels for color-image sharpening, which can be readily derived by the incorporation of the multivariable semi-variogram [46] to compute kriging weights of color images. Furthermore, for processing a large number of high-resolution images, the computing speed of the proposed method can be potentially enhanced by considering a parallel strategy for optimizing the running time of the Laplacian-based sharpening approach using graphic processing units [47].

CODE AVAILABILITY
MATLAB codes implemented in this study are available at: https://sites.google.com/view/tuan-d-pham/codes, under the name "Kriging-weighted Laplacian kernels".

REFERENCES
[1] Q. Chen, J. Xu, and V. Koltun, "Fast image processing with fully-convolutional networks," in *Proc. IEEE Int. Conf. Comput. Vis. (ICCV)*, Oct. 2017, pp. 2516–2525.
[2] I. Lauriola, C. Gallicchio, and F. Aiolli, "Enhancing deep neural networks via multiple kernel learning," *Pattern Recognit.*, vol. 101, May 2020, Art. no. 107194.
[3] X. Deng, M. A. B. Mahmoud, Q. Yin, and P. Guo, "An efficient and effective deep convolutional kernel pseudoinverse learner with multi-filter," *Neurocomputing*, vol. 457, pp. 74–83, Oct. 2021.
[4] L. Alzubaidi, J. Zhang, A. J. Humaidi, A. Al-Dujaili, Y. Duan, O. Al-Shamma, J. Santamaría, M. A. Fadhel, M. Al-Amidie, and L. Farhan, "Review of deep learning: Concepts, CNN architectures, challenges, applications, future directions," *J. Big Data*, vol. 8, no. 1, pp. 1–74, Dec. 2021.
[5] R. C. Gonzalez and R. E. Woods, *Digital Image Processing*, 4th ed. Essex, U.K.: Pearson, 2018.
[6] M. Aubry, S. Paris, S. W. Hasinoff, J. Kautz, and F. Durand, "Fast local Laplacian filters: Theory and applications," *ACM Trans. Graph.*, vol. 33, no. 5, pp. 167:1–167:14, Sep. 2014.

[7] S. Paris, S. W. Hasinoff, and J. Kautz, "Local Laplacian filters: Edge-aware image processing with a Laplacian pyramid," *Commun. ACM*, vol. 58, no. 3, pp. 81–91, Feb. 2015.

[8] H. Du, X. Jin, and P. J. Willis, "Two-level joint local Laplacian texture filtering," *Vis. Comput.*, vol. 32, no. 12, pp. 1537–1548, Dec. 2016.

[9] J. Li and Y. Li, "Guided local Laplacian filter-based image enhancement for deep-sea sensor networks," *Multimedia Tools Appl.*, vol. 77, no. 9, pp. 10823–10834, 2018.

[10] S. Yu and W. Yiquan, "An improved local Laplacian filter based on the relative total variation," *Digit. Signal Process.*, vol. 78, pp. 56–71, Jul. 2018.

[11] L. Moraru, C. D. Obreja, N. Dey, and A. S. Ashour, "Dempster–Shafer fusion for effective retinal vessels' diameter measurement," in *Soft Computing Based Medical Image Analysis*, N. Dey, A. S. Ashour, F. Shi, and V. E. Balas, Eds. London, U.K.: Academic, 2018, pp. 149–160.

[12] S.-H. Lee, H.-U. Kim, and C.-S. Kim, "ELF-Nets: Deep learning on point clouds using extended Laplacian filter," *IEEE Access*, vol. 7, pp. 156569–156581, 2019.

[13] W. Waheed, G. Deng, and B. Liu, "Discrete Laplacian operator and its applications in signal processing," *IEEE Access*, vol. 8, pp. 89692–89707, 2020.

[14] L. Zheng and W. Xu, "An improved adaptive spatial preprocessing method for remote sensing images," *Sensors*, vol. 21, no. 17, p. 5684, Aug. 2021.

[15] Y. Gong, W. Tang, and L. Zhou, "Quarter Laplacian filter for edge aware image processing," in *Proc. IEEE Int. Conf. Image Process. (ICIP)*, Sep. 2021, pp. 1959–1963.

[16] D. Marr and E. Hildreth, "Theory of edge detection," *Proc. Roy. Soc. London. B, Biol. Sci.*, vol. 207, pp. 187–217, Feb. 1980.

[17] G. E. Sotak and K. L. Boyer, "The Laplacian-of-Gaussian Kernel: A formal analysis and design procedure for fast, accurate convolution and full-frame output," *Comput. Vis., Graph., Image Process.*, vol. 48, no. 2, pp. 147–189, 1989.

[18] B. Kamgar-Parsi, B. Kamgar-Parsi, and A. Rosenfeld, "Optimally isotropic Laplacian operator," *IEEE Trans. Image Process.*, vol. 8, no. 10, pp. 1467–1472, Oct. 1999.

[19] C. Orhei, V. Bogdan, C. Bonchis, and R. Vasiu, "Dilated filters for edge-detection algorithms," *Appl. Sci.*, vol. 11, no. 22, p. 10716, Nov. 2021.

[20] P. Perona and J. Malik, "Scale-space and edge detection using anisotropic diffusion," *IEEE Trans. Pattern Anal. Mach. Intell.*, vol. 12, no. 7, pp. 629–639, Jul. 1990.

[21] G. Gerig, O. Kubler, R. Kikinis, and F. A. Jolesz, "Nonlinear anisotropic filtering of MRI data," *IEEE Trans. Med. Imag.*, vol. 11, no. 2, pp. 221–232, Jun. 1992.

[22] J. G. M. Schavemaker, M. J. T. Reinders, J. J. Gerbrands, and E. Backer, "Image sharpening by morphological filtering," *Pattern Recognit.*, vol. 33, no. 6, pp. 997–1012, Jun. 2000.

[23] M. A. Wirth and D. Nikitenko, "Fuzzy image sharpening of historical prints," in *Proc. IEEE Int. Conf. Fuzzy Syst.*, Jul. 2006, pp. 969–976, doi: 10.1109/FUZZY.2006.1681828.

[24] L. Ying, N. T. Ming, and L. B. Keat, "A wavelet based image sharpening algorithm," in *Proc. Int. Conf. Comput. Sci. Softw. Eng.*, Dec. 2008, pp. 1053–1056, doi: 10.1109/CSSE.2008.1631.

[25] H. Ibrahim and N. S. P. Kong, "Image sharpening using sub-regions histogram equalization," *IEEE Trans. Consum. Electron.*, vol. 55, no. 2, pp. 891–895, May 2009.

[26] J. Calder, A. Mansouri, and A. Yezzi, "Image sharpening via sobolev gradient flows," *SIAM J. Imag. Sci.*, vol. 3, no. 4, pp. 981–1014, Jan. 2010.

[27] I. Papamarkou, N. Papamarkos, and S. Theochari, "A novel image sharpening technique based on 2D-DWT and image fusion," in *Proc. 17th Int. Conf. Inf. Fusion (FUSION)*, Jul. 2014, pp. 1–8.

[28] J.-A. Lian, "Two adaptive schemes for image sharpening," in *Proc. IEEE 2nd Int. Conf. Inf. Commun. Technol. (ICICT)*, Mar. 2019, pp. 122–125, doi: 10.1109/INFOCT.2019.8711269.

[29] S. Khetkeeree and P. Thanakitivirul, "Hybrid filtering for image sharpening and smoothing simultaneously," in *Proc. 35th Int. Tech. Conf. Circuits/Syst., Comput. Commun. (ITC-CSCC)*, Jul. 2020, pp. 367–371.

[30] Z. Al-Ameen, M. A. Al-Healy, and R. A. Hazim, "Anisotropic diffusion-based unsharp masking for sharpness improvement in digital images," *J. Soft Comput. Decis. Support Syst.*, vol. 7, pp. 7–12, Nov. 2020.

[31] G. Matheron, "Principles of geostatistics," *Econ. Geol.*, vol. 58, no. 8, pp. 1246–1266, 1963.

[32] R. A. Olea, *Geostatistics for Engineers and Earth Scientists*. Boston, MA, USA: Kluwer, 1999.

[33] E. H. Isaaks and R. M. Srivastava, *An Introduction to Applied Geostatistics*. New York, NY, USA: Oxford Univ. Press, 1989.

[34] *Anisotropic Diffusion Based Unsharp Masking for Image Sharpening*. GitHub. Accessed: Apr. 3, 2022. [Online]. Available: https://github.com/qi-zohair/Anisotropic-Diffusion-Based-Unsharp-Masking-for-Image-Sharpening

[35] T. Birdal. *Sharpness Estimation From Image Gradients*. MATLAB Central File Exchange. Accessed: Oct. 22, 2021. [Online]. Available: https://www.mathworks.com/matlabcentral/fileexchange/32397-sharpness-estimation-from-image-gradients

[36] N. Venkatanath, D. Praneeth, B. M. Chandrasekhar, S. S. Channappayya, and S. S. Medasani, "Blind image quality evaluation using perception based features," in *Proc. 21st Nat. Conf. Commun. (NCC)*, Feb. 2015, pp. 1–6.

[37] Z. Wang, A. C. Bovik, H. R. Sheikh, and E. P. Simoncelli, "Image quality assessment: From error visibility to structural similarity," *IEEE Trans. Image Process.*, vol. 13, no. 4, pp. 600–612, Apr. 2004.

[38] S. Khandelwal, Z. Choudhury, S. Shrivastava, and S. Purini, "Accelerating local Laplacian filters on FPGAs," in *Proc. 30th Int. Conf. Field-Program. Log. Appl. (FPL)*, Aug. 2020, pp. 109–114.

[39] W. Oh and W. B. Lindquist, "Image thresholding by indicator Kriging," *IEEE Trans. Pattern Anal. Mach. Intell.*, vol. 21, no. 7, pp. 590–602, Jul. 1999.

[40] J. Ruiz-Alzola, C. Alberola-Lopez, and C. F. Westin, "Kriging filters for multidimensional signal processing," *Signal Process.*, vol. 85, pp. 413–439, 2005.

[41] T. D. Pham, "Estimating parameters of optimal average and adaptive Wiener filters for image restoration with sequential Gaussian simulation," *IEEE Signal Process. Lett.*, vol. 22, no. 11, pp. 1950–1954, Nov. 2015.

[42] R. Varatharajan, K. Vasanth, M. Gunasekaran, M. Priyan, and X. Z. Gao, "An adaptive decision based Kriging interpolation algorithm for the removal of high density salt and pepper noise in images," *Comput. Elect. Eng.*, vol. 70, pp. 447–461, Aug. 2018.

[43] M. Trumpis, C.-H. Chiang, A. L. Orsborn, B. Bent, J. Li, J. A. Rogers, B. Pesaran, G. Cogan, and J. Viventi, "Sufficient sampling for Kriging prediction of cortical potential in rat, monkey, and human μECoG," *J. Neural Eng.*, vol. 18, no. 3, Jun. 2021, Art. no. 036011.

[44] C. Liu, Q. Sun, W. Dai, Z. Ren, Q. Li, and F. Yu, "A method of camera calibration based on Kriging interpolation," *IEEE Access*, vol. 9, pp. 153540–153547, 2021.

[45] P. Goovaerts, "Kriging and semivariogram deconvolution in the presence of irregular geographical units," *Math. Geosci.*, vol. 40, no. 1, pp. 101–128, 2008.

[46] G. Bourgault and D. Marcotte, "Multivariable variogram and its application to the linear model of coregionalization," *Math. Geol.*, vol. 23, no. 7, pp. 899–928, Aug. 1991.

[47] T. Ma, L. Li, S. Ji, X. Wang, Y. Tian, A. Al-Dhelaan, and M. Al-Rodhaan, "Optimized Laplacian image sharpening algorithm based on graphic processing unit," *Phys. A, Stat. Mech. Appl.*, vol. 416, pp. 400–410, Dec. 2014.

TUAN D. PHAM (Senior Member, IEEE) is currently a Senior Research Professor in artificial intelligence and the Founding Director of the Center for Artificial Intelligence, Prince Mohammad Bin Fahd University, Saudi Arabia. He was a Professor of biomedical engineering at Linkoping University, Sweden, a Professor and the Leader at the Aizu Research Cluster for Medical Engineering and Informatics and the Medical Image Processing Laboratory, University of Aizu, Japan, and an Associate Professor and the Bioinformatics Research Group Leader at the University of New South Wales, Canberra, Australia. His current research interests include AI and machine learning methods for image processing, time-series analysis, complex networks, and pattern recognition with applications to medicine, biology, and mental health. He is a long-serving Associate Editor of *Pattern Recognition*, and IEEE-EMBC (Theme 10: Biomedical and Health Informatics). He was selected in 2020 as an Expert in artificial intelligence for consultation by the U.S. Food and Drug Administration (FDA) Center for Devices and Radiological Health (CDRH) Network of Digital Health Experts Program (NoDEx). He is a Full Member of Sigma Xi—The Scientific Research Honor Society.

● ● ●